Anthropogenic aerosols have significantly weakened the regional summertime circulation in the Northern Hemisphere during the satellite era

Joonsuk M. Kang[1], Tiffany A. Shaw[1], Lantao Sun[2]

[1]Department of the Geophysical Sciences, The University of Chicago, Chicago, IL, 60637
[2]Department of Atmospheric Sciences, Colorado State University, Fort Collins, CO, 80521

Key Points:

- Aerosol forcing has significantly weakened the regional summertime circulation in the Northern Hemisphere and dominates in the Pacific.
- Aerosol-induced shortwave radiation trends are largest over Eurasia and result in energy export to the ocean via stationary circulation.
- Aerosol-induced energy export from land weakens the storm track over the ocean, particularly in the Pacific.

Corresponding author: Joonsuk M Kang, jmkang@uchicago.edu

Abstract

Reanalysis data show a significant weakening of summertime circulation in the Northern Hemisphere midlatitudes in the satellite era with important implications for surface weather extremes. Recent work showed the weakening is not significantly affected by changes in the Arctic, but did not examine the role of different anthropogenic forcings such as aerosols. Here we use the Detection and Attribution Model Intercomparison Project (DAMIP) simulations to quantify the impact of anthropogenic aerosol and greenhouse gas forcing. The DAMIP simulations show aerosols and greenhouse gases contribute equally to zonal-mean summertime circulation weakening. Regionally, aerosol dominates the Pacific storm track weakening whereas greenhouse gas dominates the Atlantic. Using a regional energetic framework, we interpret how aerosol forcing weakens the storm tracks and why the impact is the largest in the Pacific. Decreasing aerosol emissions over Eurasia and North America increases (clear-sky) shortwave radiation. The atmospheric energy input is exported downstream via stationary circulation, poleward of the Pacific and Atlantic storm tracks. This land-ocean energy coupling is similar to the spring-to-summer seasonal transition and is larger over the Pacific due to greater energy input over Eurasia. In addition, increasing aerosol emissions over South and East Asia decreases shortwave radiation, and the energy export downstream via stationary circulation weakens. This occurs equatorward of the Pacific storm track, which further weakens it. Our results show aerosols are a dominant driver of regional circulation trends during the Northern Hemisphere summertime in the satellite era and show a regional energetic framework explaining the underlying processes.

Plain Language Summary

Over the last four decades, Northern Hemisphere summertime westerlies and weather systems have weakened. While this has important implications for weather and its extremes, how different anthropogenic forcings, such as aerosols and greenhouse gases, have impacted the weakening is currently unclear. Using coordinated climate model simulations, we show anthropogenic aerosols are as important as greenhouse gases for the weakening of the weather systems and the most important over the Pacific. Efforts to reduce aerosol emissions over North America and Europe increased the solar energy reaching the surface, whereas heightened pollution from Asia decreased the solar energy reaching the surface. As a result, energy increases at higher latitudes and decreases at lower latitudes, weakening the equator-to-pole energy (temperature) difference consistent with weaker weather systems. This effect is greater in the Pacific. Our results emphasize that how aerosol emissions will evolve in the future has important implications for regional climate change.

1 Introduction

Climatologically, the Northern Hemisphere (NH) midlatitude circulation is the weakest during summertime (Shaw et al., 2018; Hoskins & Hodges, 2019). Under anthropogenic forcing, the NH summertime circulation is projected to become weaker over the 21st century (O'Gorman, 2010; Coumou et al., 2015; Shaw & Voigt, 2015; Shaw et al., 2018; Harvey et al., 2020). Over the satellite era (1980 to present), reanalysis data show a statistically significant weakening of the zonal-mean NH summertime circulation, including storm tracks and jets (Coumou et al., 2015; Chang et al., 2016; Gertler & O'Gorman, 2019; Dong et al., 2022; Kang et al., 2023; Chemke & Coumou, 2024). The weakening of the summertime midlatitude circulation implies more persistent summertime weather (Pfleiderer et al., 2019), which could have an important influence on temperature extremes (Lehmann & Coumou, 2015; Chang et al., 2016) and local air quality (Leibensperger et al., 2008). Hence, it is essential to understand the drivers and mechanisms responsible for the weakening of the regional circulation during the NH summertime.

The weakening of the NH summertime circulation in the satellite era has been hypothesized to be related to Arctic Amplification which weakens the equator-to-pole temperature gradient (Coumou et al., 2015, 2018). However, Kang et al. (2023) used climate model simulations with nudged Arctic sea ice to show that Arctic Amplification does not significantly contribute to the summertime circulation weakening in the satellite era. Instead, Kang et al. (2023) suggests anthropogenic forcing in the absence of Arctic Amplification or Arctic sea ice loss dominates the circulation weakening. Anthropogenic forcings include direct CO_2 radiative forcings (Shaw & Voigt, 2015, 2016; Shaw et al., 2018) and aerosols (Dong & Sutton, 2021; Dong et al., 2022).

Both CO_2 direct radiative and aerosol forcings directly impact the energy balance over land and thereby affect the summertime circulation. For example, Shaw et al. (2018) revealed that direct CO_2 radiative forcing over high latitude land weakens the NH summertime zonal-mean storm tracks by increasing local surface turbulent fluxes (see Fig. 1c in Shaw & Voigt, 2016) and thereby weakening the equator-to-pole energy gradient. Dong et al. (2022) demonstrated that anthropogenic aerosol forcing has induced high-latitude warming and low-latitude cooling across the Eurasian continent, which through thermal wind balance leads to a weakening of the summertime Eurasian jet. Chemke and Coumou (2024) reported aerosols and greenhouse gases both contribute to weakening zonal-mean storm tracks in CESM2 (Danabasoglu et al., 2020). However, it is currently unclear how aerosols, which are very regional and lead to radiative forcing mainly over land, impact the circulation trends downstream (over ocean or other land regions).

Anthropogenic aerosol can impact atmospheric circulation through aerosol-radiation and/or aerosol-cloud effects (Ming & Ramaswamy, 2009; Allen & Sherwood, 2011; Ming et al., 2011; Wang et al., 2014; Shen & Ming, 2018; Dong et al., 2022), mediated by ocean-atmosphere interactions (Xie et al., 2013). In the satellite era, the primary feature of aerosol emissions change is the decrease in sulfate aerosols (shortwave reflectors) over Europe and North America, and the increase over South and East Asia (Klimont et al., 2013; Hoesly et al., 2018; Quaas et al., 2022). The direct effects from these emission changes are spatially inhomogeneous clear-sky surface shortwave trends that are opposite to the aerosol emission trends (Diao et al., 2021; Dong et al., 2022; Schumacher et al., 2024). Previous work studied how the spatially inhomogeneous shortwave radiation changes impact the annual-mean circulation (Wang et al., 2015; Diao et al., 2021; Kang et al., 2021; Needham & Randall, 2023), and showed that they can induce different surface temperature trends over the Pacific and Atlantic oceans (Diao et al., 2021; Kang et al., 2021). However, it is currently unclear how aerosol changes impact the regional circulation during NH summertime and what the underlying mechanisms are.

In this study, our objective is to quantitatively assess the impact of anthropogenic aerosols on the weakening of the NH summertime circulation, with a specific focus on storm tracks. To achieve this, we address the following questions. (1) How do different anthropogenic forcings impact the regional summertime circulation weakening in the satellite era? Do they have the same impact on the Pacific and Atlantic storm tracks? (2) What is the physical mechanism connecting regional aerosol changes over land to circulation trends during NH summertime? Is the mechanism similar to other shortwave radiation forcing, for example, the response to Arctic sea ice loss or the seasonal transition, which weakens the circulation by decreasing the equator-to-pole energy gradient (Shaw et al., 2018; Shaw & Smith, 2022; Kang et al., 2023)? The questions are answered using the CMIP6 Detection and Attribution Model Intercomparison Project (DAMIP, Gillett et al., 2016) simulations and using a regional energetic framework that connects the atmospheric circulation to the shortwave radiation trends induced by regional aerosol emissions.

2 Data and Methods

2.1 Reanalysis datasets

We use reanalysis datasets to quantify the circulation trends in the satellite era. To account for observational uncertainty (Schmidt, 2013; Kang et al., 2024), we use four reanalysis datasets: CFSR/CFSv2 (Saha et al., 2010, 2014), JRA55 (Kobayashi et al., 2015), MERRA2 (Gelaro et al., 2017), and ERA5 (Hersbach et al., 2020), which are the latest datasets from different reanalysis centers.

2.2 CMIP6 DAMIP simulations

We use the CMIP6 DAMIP (Gillett et al., 2016) simulations to quantitatively separate the role of anthropogenic aerosols from greenhouse gas forcing on the summertime circulation trends in the satellite era. The single forcing simulations for anthropogenic aerosol (hist-aer, hereafter AER), greenhouse gas (hist-GHG, hereafter GHG), and natural forcing (hist-nat, hereafter NAT) are compared with the historical (1980–2014) and SSP245 (2015–2020) simulations (hereafter ALL for all forcing) in the CMIP6 ScenarioMIP (Eyring et al., 2016).

To answer the first series of questions, we use all models and realizations that have daily mean variables to quantify circulation trends across all ALL, GHG, AER, and NAT simulations. For zonal and meridional winds at pressure levels, there are 35 simulations from 8 models, and for sea-level pressure, there are 43 simulations from 11 models (Table S1). To answer the second series of questions, we utilize 26 simulations from 5 models that have daily-mean meridional wind, temperature, geopotential, and specific humidity in AER simulations (Table S1). The ensemble mean is created by taking an average across all simulations. Although different models have different numbers of realizations, the results are consistent if we first average across different realizations in different models and then take the multi-model mean, as we show later. The ensemble-mean trend likely represents the forced response to individual forcings, and the ensemble spread represents both structural uncertainty and internal variability (Deser et al., 2020).

2.3 Summertime circulation metrics

To answer the first series of questions, we evaluate the summertime circulation trends using various metrics across reanalyses and DAMIP simulations. We specifically focus on those documented in previous work and available across a sufficient number of simulations, which are as follows.

We quantify summertime (June-July-August) storm tracks using two different metrics. First, we use vertically integrated eddy kinetic energy (hereafter EKE) defined as follows (Kang et al., 2023):

$$EKE = \frac{1}{g}\int_{p_s}^{10\mathrm{hPa}} \frac{\overline{u'^2 + v'^2}}{2} dp. \tag{1}$$

Here, the overbar denotes the monthly mean and the primes denote deviations therefrom. Note that daily-mean u and v are used and vertical integration is performed along selected 8 pressure levels available in the DAMIP simulations (1000, 850, 700, 500, 250, 100, 50, and 10 hPa). We use daily-mean surface pressure (p_s), but this is replaced with monthly mean when unavailable.

The second metric for storm track intensity is the extratropical cyclone activity (hereafter ECA, Chang et al., 2016; Gertler et al., 2020) representing 24-hour sea-level pressure (SLP) variance defined as follows:

$$ECA = \overline{(\mathrm{SLP(t + 24hrs)} - \mathrm{SLP(t)})^2}, \tag{2}$$

where SLP(t) is daily-mean SLP. Compared to EKE, ECA represents storm track intensity near the surface.

In addition to storm track metrics, we quantify the summertime jet trends with zonal wind at 500 hPa pressure level (hereafter U500 e.g., Coumou et al., 2015). Our results for U500 trends are broadly consistent with Dong et al. (2022), who documented zonal wind trends at 200 hPa.

All circulation trends from 1980 to 2020 are quantified as the slope of least-squares fit linear regression, and the statistical significance is evaluated as the 95% confidence level using a two-sided Student's t-test.

2.4 Energetic framework for regional storm tracks

In order to understand the connection between aerosol forcing, which induces trends in surface shortwave radiation, and the storm tracks, we use the moist static energy (MSE) framework. The MSE framework has been successfully used to explain the zonal-mean storm track response to changes in shortwave radiation induced by sea ice loss (Shaw & Smith, 2022), the seasonal cycle (Barpanda & Shaw, 2020), as well as the impact of topography and the ocean circulation (Shaw et al., 2022). Specifically, the MSE framework connects surface shortwave radiation and storm track intensity by considering surface energy and atmospheric MSE budget equations.

Previous work showed that aerosol forcing impacts the surface energy budget through trends in surface shortwave radiation (Diao et al., 2021; Dong et al., 2022). The surface shortwave radiation trends impact surface turbulent flux trends via the surface energy balance (e.g. Shaw & Smith, 2022; Kang et al., 2023):

$$TF = SW_s + LW_s + NA, \tag{3}$$

where TF is surface turbulent fluxes, SW_s is the surface shortwave radiation, LW_s is the surface longwave radiation, and NA is the non-atmospheric fluxes (e.g., surface heat storage and ocean heat flux divergence).

The surface turbulent flux trends can then impact the trends in the atmospheric MSE (denoted m) budget (Kang et al., 2008; Shaw & Smith, 2022):

$$\underbrace{\nabla \cdot \mathbf{F_{TE}} + \nabla \cdot \mathbf{F_{SC}}}_{\nabla \cdot \mathbf{F}} + \underbrace{\nabla \cdot \mathbf{F}_{\partial_t\{\mathbf{h}\}}}_{\partial_t\{h\}} = \underbrace{\nabla \cdot \mathbf{F_{Ra}}}_{Ra} + \underbrace{\nabla \cdot \mathbf{F_{TF}}}_{TF}, \tag{4}$$

where $\mathbf{F_{TE}} = (F^x_{TE}, F^y_{TE}) = (\overline{\{u'm'\}}, \overline{\{v'm'\}})$ and $\mathbf{F_{SC}} = (F^x_{SC}, F^y_{SC}) = (\{\bar{u}\bar{m}\}, \{\bar{v}\bar{m}\})$ are vertically integrated (denoted $\{\cdot\}$) atmospheric MSE flux vectors due to transient eddies (storm tracks) and stationary circulations, respectively. Here the stationary circulations include stationary waves, jet stream, and mean meridional circulations. Then, $\nabla \cdot \mathbf{F}$ is the total atmospheric MSE flux divergence. The other terms are in flux form with their global mean removed, $\nabla \cdot \mathbf{F}_{\partial_t\{\mathbf{h}\}} = \partial_t\{h\}$, $\nabla \cdot \mathbf{F_{Ra}} = Ra$ and $\nabla \cdot \mathbf{F_{TF}} = TF$, where $\partial_t\{h\}$ is the atmospheric heat storage (h is the moist enthalpy), Ra is the radiative cooling, and TF is surface turbulent fluxes. To ensure mass continuity, $\nabla \cdot \mathbf{F_{TE}}$ is calculated following Donohoe and Battisti (2013) and $\nabla \cdot \mathbf{F_{SC}}$ is calculated as a residual. Note that all terms are in units of W m^{-2}. The surface turbulent flux (TF) connects Eqs. (3) and (4), and therefore quantitatively connects surface shortwave radiation (SW_s) to the MSE flux divergence due to storm tracks ($\nabla \cdot \mathbf{F_{TE}}$).

Previous work defined zonal-mean storm track intensity, using the meridional component of $\mathbf{F_{TE}}$, as $[2\pi a \cos\phi F^y_{TE}]$, where $[\cdot]$ is the zonal mean and a is the Earth's radius (Shaw et al., 2018; Shaw & Smith, 2022). Using this zonal-mean definition, the contribution of different terms in Eq. (4) to the storm track intensity can be quantified.

We define regional storm track intensity, using the meridional component of $\mathbf{F}^{\star}_{\mathbf{TE}}$, as $2\pi a\cos\phi F^{y,\star}_{TE}$, where superscript $\star$ denotes the divergent component of a vector. This definition of regional storm track intensity is useful since the divergent component ($2\pi a\cos\phi F^{y,\star}_{TE}$) dominates $2\pi a\cos\phi F^{y}_{TE}$ (Fig. S1). The procedure of calculating storm track intensity $2\pi a\cos\phi F^{y,\star}_{TE}$ from $\nabla\cdot\mathbf{F_{TE}}$ can be expressed as (see also Boos & Korty, 2016; Nicknish et al., 2023):

$$2\pi a\cos\phi F^{y,\star}_{TE} = 2\pi a\cos\phi\partial_y\nabla^{-2}(\nabla\cdot\mathbf{F_{TE}}). \tag{5}$$

Then, using Eq. (5), we obtain an equation for regional storm track intensity from Eq. (4):

$$2\pi a\cos\phi F^{y,\star}_{TE} = 2\pi a\cos\phi(F^{y,\star}_{Ra} + F^{y,\star}_{TF} - F^{y,\star}_{SC} - F^{y,\star}_{\partial_t\{h\}}), \tag{6}$$

where $F^{y,\star}_{Ra}$, $F^{y,\star}_{TF}$, $-F^{y,\star}_{SC}$, and $-F^{y,\star}_{\partial_t\{h\}}$ respectively represents the contribution of radiative cooling, surface turbulent flux, stationary circulation, and atmospheric heat storage to the storm track intensity. Thus, Eq. (6) quantifies how the terms in the MSE budget (Eq. 4) impact regional storm track intensity. All terms have a unit of PW and are defined at every longitude and latitude.

3 Results

3.1 Impact of anthropogenic forcings on summertime circulation weakening

3.1.1 Zonal-mean trends

The summertime circulations quantified by EKE, ECA, and U500 weaken in the satellite era across reanalysis datasets (black, Figs. 1a–c), consistent with trends reported in previous work (Coumou et al., 2015; Chang et al., 2016; Gertler & O'Gorman, 2019; Dong et al., 2022; Kang et al., 2023). The weakening trends in reanalysis datasets are statistically significant across most metrics (Figs. 1d–f). The average EKE, ECA, and U500 trends in four reanalyses correspond to weakening of -1.3% decade^{-1}, -1.9% decade^{-1}, and -0.8% decade^{-1}, respectively.

Similar to the reanalyses, EKE, ECA, and U500 all weaken in the ALL simulations (purple, Figs. 1a–c) showing DAMIP simulations have skill in simulating the circulation weakening. For all metrics, the ensemble-mean trends in ALL simulations are close to the average of reanalysis trends (black and purple, Figs. 1d–f). Furthermore, if we give each reanalysis trend a percentile rank in the model ensemble distribution (cf. Kang et al., 2024), the average reanalysis ranks in the ALL simulation ensemble are 39.3%, 40.3%, and 50.0% for EKE, ECA, and U500, respectively. This indicates that reanalysis trends sit squarely within the trend distribution of ALL simulation ensemble and thus the ALL simulation ensemble captures the circulation trends in reanalyses.

As the ALL simulations capture the reanalyses circulation trends, we now quantify how much of the weakening is attributable to individual forcings. The ensemble-mean EKE trends in GHG (red, Fig 1d) and AER (blue, Fig 1d) simulations are statistically significant and represent 44.6% and 37.8% of the total weakening trend, respectively. The results do not change if we first average across different realizations in different models and then take the multi-model mean (Fig. S2). Similarly, for ECA, the ensemble-mean trends in GHG (red, Fig. 1e) and AER (blue, Fig. 1e) simulations are statistically significant and respectively represent 45.5% and 46.5% of the total weakening trend. For U500, the ensemble-mean trends in GHG (red, Fig. 1f) and AER (blue, Fig. 1f) simulations are also statistically significant, and respectively represent 32.3% and 63.6% of the total weakening trend. For all metrics, the ensemble-mean trends in NAT simulations are small and statistically insignificant (brown, Figs. 1d–f). The sum of ensemble-mean trends in the single forcing simulations is close to the ALL simulation ensemble-mean trend, indicating the linearity of circulation responses to individual forcings (magenta line and purple bar Figs. 1d–f).

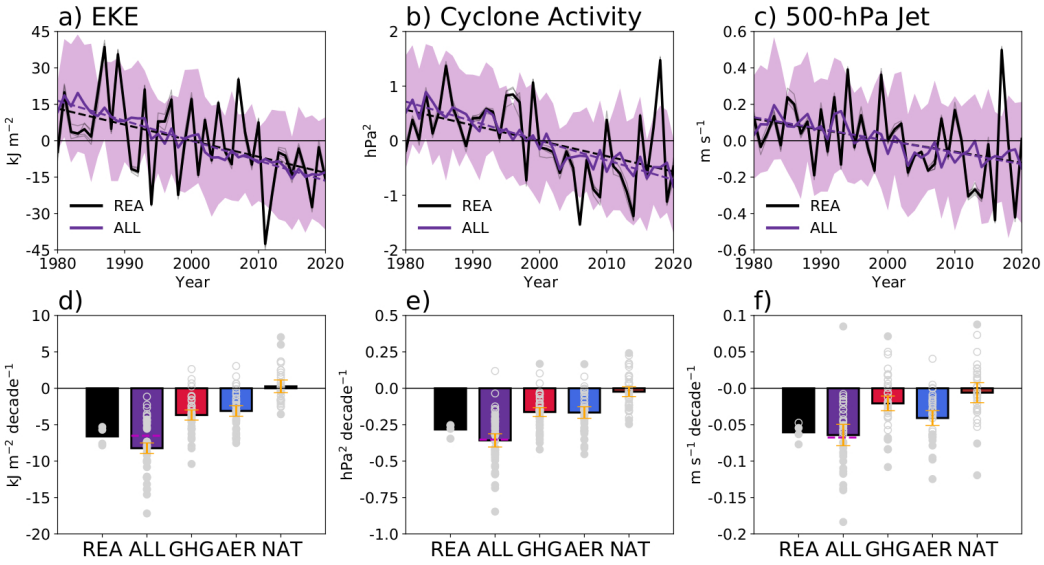

Figure 1. (a–c) Timeseries of NH JJA (a) EKE (30–60°N), (b) ECA (30–70°N), and (c) U500 (35–70°N) for reanalysis (black) and ALL simulation ensemble mean (purple) with respect to 1980–2020 climatology. The corresponding linear regressions are shown in dashed lines. The timeseries in individual reanalysis are shown in thin black lines and the 10–90 % model ensemble spread is shaded. (d–f) Linear trends of NH JJA (d) EKE, (e) ECA, and (f) U500 from 1980 to 2020 in reanalysis data and DAMIP simulations. The reanalysis and ensemble mean trends are shown in bars and individual reanalysis and simulation trends are shown in gray circles. The circles are filled if the trends are statistically significant at the 95% confidence level. The 95% confidence intervals for the ensemble mean trend are shown with yellow errorbars. The magenta line indicates the sum of ensemble-mean trends in the single forcing simulations.

3.1.2 Regional trends

The storm track weakening, throughout the troposphere (EKE) and at the surface (ECA), exhibits a regional structure with a clear weakening over storm tracks in the Pacific and Atlantic sectors in reanalysis data (Fig. 2a and Fig. 3a). The ALL simulations also exhibit a weakening of Pacific and Atlantic storm tracks in the ensemble mean (Figs . 2b and 3b). The U500 also weakens over Eurasia and the Pacific consistent with Dong et al. (2022), and it weakens with an equatorward shift over the Atlantic (Fig. S3).

Some differences in the spatial structure between the reanalyses and ensemble mean trends are expected because the ensemble mean is an average across different realizations and the reanalysis mean represents a single realization. The positive ECA trends in reanalysis over the Atlantic (Fig. 3a) are consistent with Atlantic U500 trends that could steer surface cyclones more toward Europe, which is not well represented in the ALL simulations (Fig. S3, see also Dong & Sutton, 2021). When considering the Pacific and Atlantic storm track weakening separately, the ensemble-mean trends are close to the reanalyses trends (black and purple, Figs. 2e and f and Figs. 3e and f). The average reanalysis ranks for EKE trends are 30.7% and 55.7% in the ALL simulation ensemble for the Pacific and Atlantic, respectively. The corresponding average reanalysis ranks are also similar for ECA trends (32.0% and 69.3%), indicating that the ALL simulations capture the regional reanalysis storm track trends.

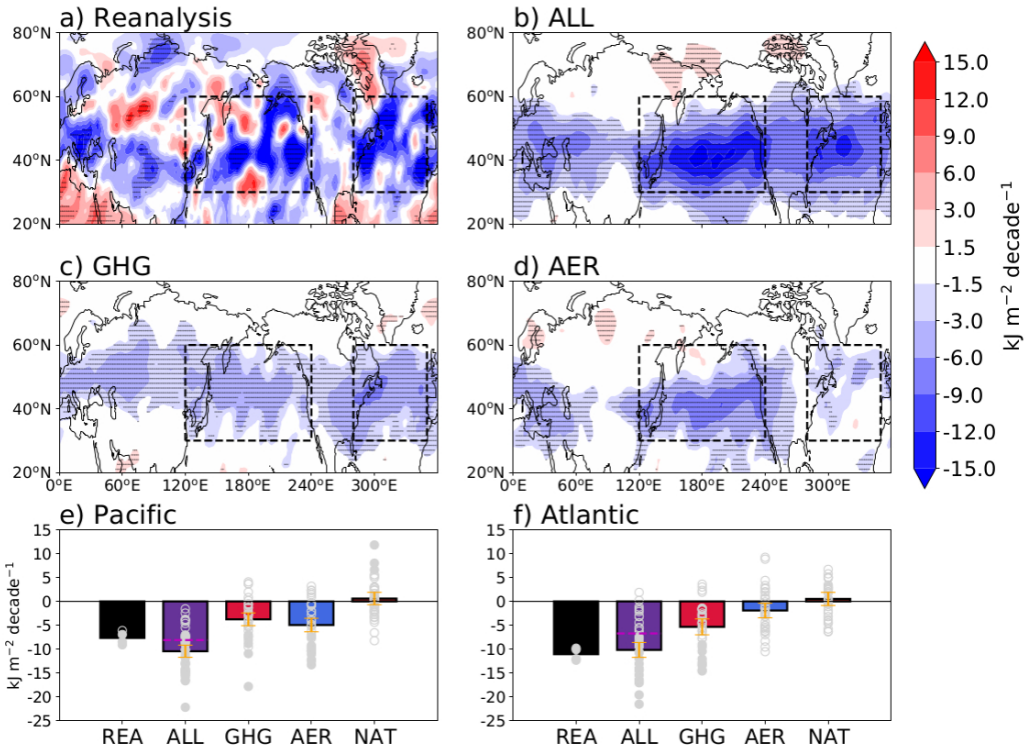

Figure 2. (a–d) Spatial structure of JJA EKE trends from 1980 to 2020 in (a) reanalyses mean (CFSR, ERA5, JRA55, and MERRA2) and ensemble-mean (b) ALL, (c) GHG, and (d) AER simulations. Statistically significant trends at the 95% confidence level are stippled. Black dashed lines represent Pacific (30–60°N, 120–240°E) and Atlantic (30–60°N, 280–350°E) storm track domains, respectively. (e, f) Similar results to Fig. 1d, but for EKE trends averaged in the (e) Pacific and (f) Atlantic storm tracks.

The impacts of greenhouse gas and aerosol forcing on the storm tracks vary regionally (Figs. 2c and d and Figs. 3c and d). In response to greenhouse gas forcing, the Pacific and Atlantic storm tracks weaken similarly for both EKE and ECA (Figs. 2c,e,f and 3c,e,f). By contrast, in response to aerosol forcing, the storm track weakening in the Pacific is greater than the Atlantic (statistically significant at the 95% level) by 2.6 times for EKE and 1.8 times for ECA (Figs. 2d–f and 3d–f).

Consistently, aerosol forcing dominates the weakening of the Pacific storm track, contributing to 47.4% of the total EKE weakening and 57.1% of the total ECA weakening (blue, Figs. 2e and 3e). Greenhouse gas forcing, which contributes to 35.9% for EKE and 26.7% for ECA weakening, is secondary (red, Figs. 2e and 3e). Greenhouse gas forcing dominates the weakening of the Atlantic storm track, contributing to 52.5% of the total EKE weakening and 50.1% of the total ECA weakening (red, Figs. 2f and 3f). The contribution of aerosols to the Atlantic storm track weakening is only 18.9% for EKE and 40.8% for ECA trends (red, Figs. 2f and 3f). The ensemble-mean EKE and ECA trends in the NAT simulations are still small and insignificant for both the Pacific and Atlantic sectors. Note that circulation responses to forcings are less linear regionally (magenta dashed lines, Figs. 2e and f and Figs. 3e and f).

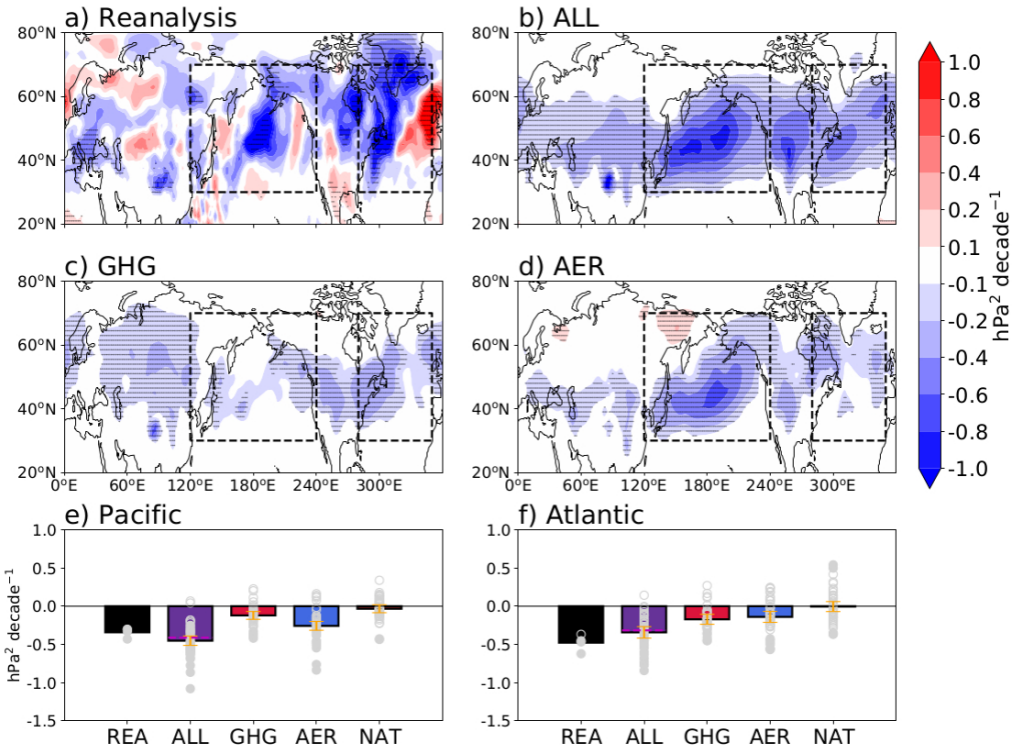

Figure 3. Similar results to Fig. 2, but for ECA trends. Black dashed lines represent Pacific (30–70°N, 120–240°E) and Atlantic (30–70°N, 280–350°E) storm track domains, respectively.

3.2 Understanding the aerosol-induced storm track weakening in the satellite era

The results above show that greenhouse gas and aerosol forcings have significantly weakened the regional storm tracks in the satellite era. The storm track weakening from greenhouse gas forcing, which is close to being zonally symmetric, has been discussed in

Shaw et al. (2018). Here we investigate how anthropogenic aerosol forcing in the satellite era has weakened the NH summertime storm tracks, especially over the Pacific. We use the regional energetic framework (Eqs. 4–6) to understand the energetic response to aerosol forcing. We analyze the ensemble-mean trends in the AER simulations in order to focus on the storm track response to aerosol forcing. Specifically, we investigate how (i) aerosol emission trends over land impact the storm tracks downstream and (ii) why the storm track weakening is greater over the Pacific sector than the Atlantic sector (Figs. 2d and 3d).

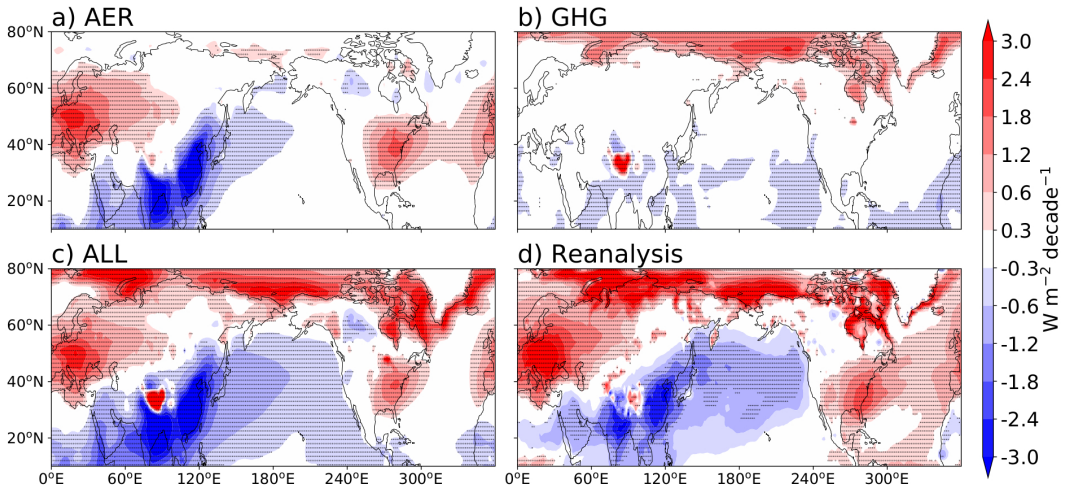

Figure 4. Spatial structure of JJA cosine-weighted trend from 1980 to 2020 of clear-sky surface shortwave radiation in ensemble-mean (a) AER, (b) GHG and (c) ALL simulations, and in (d) reanalysis (ERA5). Statistically significant trends at the 95% confidence level are stippled.

3.2.1 Surface energy budget trends

In response to aerosol forcing, clear-sky surface shortwave radiation shows a positive trend over the Eurasian continent from Europe to central Asia (hereafter Eurasia) and North America and shows a negative trend over South and East Asia (Fig. 4a). This pattern is consistent with aerosol emissions and aerosol optical depth trends in these regions (Klimont et al., 2013; Quaas et al., 2022). By contrast, greenhouse gas forcing drives a positive shortwave radiation trend over the Arctic and Tibetan Plateau but has minimal impact over most of NH land (Fig. 4b). The aerosol forcing dominates the clear-sky surface shortwave radiation trends over NH land in the ALL simulation ensemble (Fig. 4c, see also Dong et al., 2022), which reasonably reproduces the trends in reanalysis (Fig. 4d). Similar pattern of trends are also found at the top of the atmosphere (Fig. S4).

The all-sky surface shortwave radiation trends due to aerosol forcing (Fig. 5a) strongly resemble the clear-sky radiation trends (Fig. 4a). In particular, the spatial pattern correlation coefficient between the clear-sky and all-sky surface shortwave radiation trends is 0.93 over 10°–70°N. The clear-sky radiation contributes to about 65% of increasing surface shortwave radiation trends over Eurasia and North America and contributes to about 100% of decreasing surface shortwave radiation trends over South and East Asia. This indicates that the direct aerosol effect dominates the response to aerosol forcing.

The trends in (all-sky) surface shortwave radiation over Eurasia, North America, and South and East Asia are balanced by surface turbulent flux trends (Fig. 5b) accord-

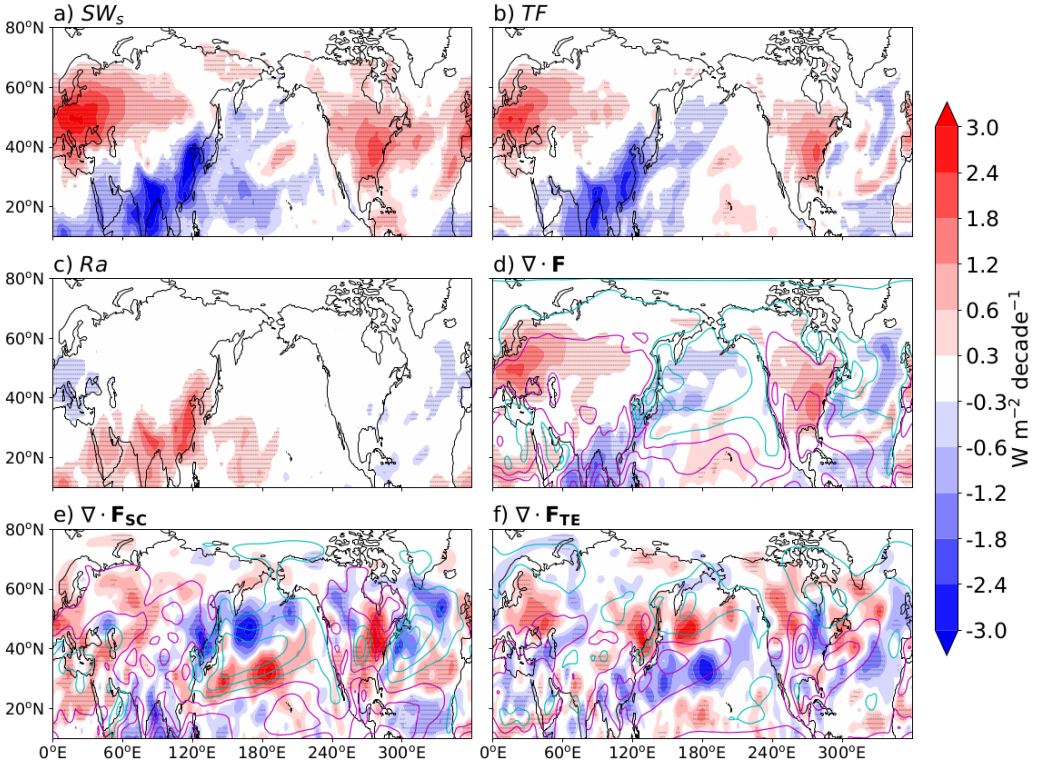

Figure 5. Spatial structure of JJA cosine-weighted ensemble-mean trends from 1980 to 2020 of (a) all-sky surface shortwave radiation, (b) surface turbulent flux, (c) radiative cooling, (d) MSE flux divergence, (e) MSE flux divergence due to stationary circulations, and (f) MSE flux divergence due to transient eddies in the AER simulations with global mean removed. Statistically significant trends at the 95% confidence level are stippled. In (d)–(f), summertime climatology is shown in magenta and cyan contours for MSE flux divergence and convergence, respectively (from 15 W m^{-2} in 30 W m^{-2} intervals), and the trends are smoothed at T63 using a filter from Sardeshmukh and Hoskins (1984).

ing to the surface energy budget with roughly equal contributions from latent and sensible heat flux. The spatial pattern correlation coefficient between surface shortwave radiation and turbulent flux trends is 0.87 over 10°–70°N. In other words, $\Delta TF \approx \Delta SW_s \approx \Delta SW_{s,clearsky}$ from Eq. (3), where Δ denotes the linear trend. Interestingly, a similar surface energy balance was seen in response to Arctic sea ice loss except in that case the balance is over the ocean (Shaw & Smith, 2022). The surface turbulent flux trends spatially integrated over the area with positive trends are 2.4 times larger in Eurasia (40°–70°N) than in North America (30°–60°N), due to larger area of decreased emissions in Eurasia (Figs. 6a and b).

3.2.2 Atmospheric MSE budget trends

The atmospheric MSE budget (Eq. 4) dictates the surface turbulent flux trend over land due to changes in the surface shortwave radiation must be balanced by changes in radiative cooling (Ra), atmospheric heat storage ($\partial_t\{h\}$), and/or atmospheric MSE flux divergence ($\nabla \cdot \mathbf{F}$). Over Eurasia and North America, the positive surface turbulent fluxes trends are balanced mostly by MSE flux divergence trend (Fig. 5d), which is dominated primarily by the stationary circulation (Fig. 5e and red in Figs. 6a and b). Consistent with surface energy budget trends, the MSE flux divergence trend due to stationary circulations ($\nabla \cdot \mathbf{F_{SC}}$) integrated over positive surface turbulent flux trends is about 2 times larger over Eurasia than North America (red in Figs. 6a and b).

Over South and East Asia, the negative surface turbulent flux trends are largely compensated by a negative radiative cooling trend (Fig. 5c and pink, Fig. 6c), followed by MSE flux convergence trend (Fig. 5d). The negative radiative cooling (i.e., radiative warming) trend is consistent with increasing shortwave-absorbing aerosol (e.g., black carbon) emissions in the region (Hoesly et al., 2018). The atmospheric MSE flux convergence trend is also dominated by stationary circulations ($\nabla \cdot \mathbf{F_{SC}}$), similar to other regions (Fig. 5e and red in Fig. 6c).

Thus, in all three land regions, aerosol-induced surface shortwave radiation trends are balanced by surface turbulent flux trends indicating trends in energy input to the atmosphere (Figs. 5a and b). Then, the surface turbulent flux trends are balanced by atmospheric MSE flux divergence/convergence ($\nabla \cdot \mathbf{F}$) trends, which is mostly due to stationary circulations ($\nabla \cdot \mathbf{F_{SC}}$, Figs. 5b–e and Figs. 6a–c). Over South and East Asia, radiative cooling mainly compensates for the surface turbulent flux trends but there still are significant MSE flux convergence trends due to stationary circulation (Fig. 5e and Fig. 6c).

The MSE flux divergence trends over the land lead to MSE flux convergence trends over the ocean downstream at similar latitudes (Fig. 5d). These trends exhibit the same sign as MSE flux divergence/convergence trends due to stationary circulations (Fig. 5e), with the latter showing larger magnitudes. Specifically, there are significant MSE flux convergence trends due to stationary circulations poleward of 40°N (Fig. 5e and Figs. 6a,b). These convergence trends integrated over these ocean sectors have a similar magnitude as divergence trends integrated over upstream land (compare red bars in Figs. 6a,b and d,e), resulting in stronger trends over the Pacific. It is useful to note that the Pacific and Atlantic oceans have a comparable area between 40–70°N, such that the difference in area integrated trends is consistent with per unit area trends (Fig. 5e and Figs. 6a,b). In addition, there also is a significant MSE flux divergence trend due to stationary circulations equatorward of 40°N in the Pacific sector (Figs. 5e and 6f), which can be connected to MSE flux convergence due to stationary circulations over South and East Asia (Fig. 6c). Thus, there is a strong meridional dipole of MSE flux convergence and divergence trends due to stationary circulations over the Pacific (Fig. 5e). Overall, the MSE flux divergence/convergence trends due to stationary circulations over land and ocean

indicate land-to-ocean MSE flux increases at latitudes where land surface turbulent flux increases and decreases at latitudes where land surface turbulent flux decreases.

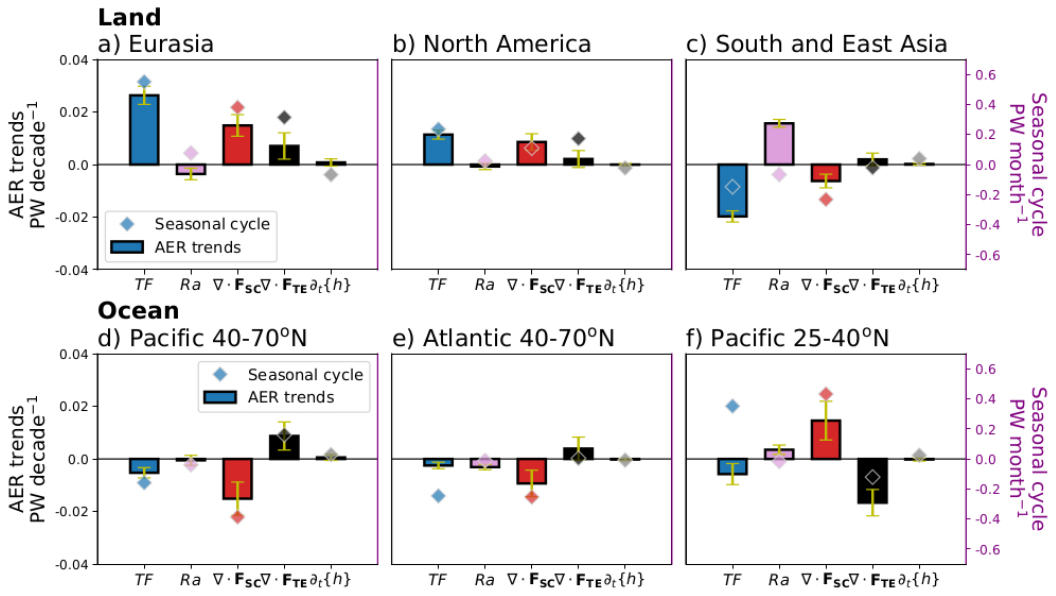

Figure 6. (bars, left axis) Ensemble-mean JJA trends (1980–2020) in the AER simulations and (diamonds, right axis) seasonal transition in ERA5 of the MSE budget integrated across (a–c) upstream land and (d–f) downstream ocean: (a) Eurasia land (40–70°N) where $\Delta TF > 0$, (b) North America land (30–60°N) where $\Delta TF > 0$, (c) South and East Asia land (10–40°N, 60–140°E) where $\Delta TF < 0$, (d) Pacific 40–70°N, (e) Atlantic 40–70°N, and (f) Pacific 25–40°N. The 95% confidence intervals for the ensemble-mean trend are shown with yellow errorbars. In (a,b) and (d,e), the seasonal transition is shown for June minus May and in (c, f) it is shown for December minus November.

The MSE flux divergence/convergence trends due to stationary circulations due to aerosol forcing in the ocean sectors are compensated by the MSE flux divergence/convergence trends due to transient eddies (Figs. 5e, f and Figs. 6d–f). The spatial correlation coefficient between the two MSE flux divergence/convergence trends is −0.91 in the ocean sectors between 20°–70°N. The compensation leads to an MSE flux divergence trend on the poleward side and a convergence trend on the equatorward side due to transient eddies, also particularly strong in the Pacific sector. This pattern of divergence and convergence trends are opposite of the climatology (cyan and magenta lines, Fig. 5f), which implies storm track weakening.

The trends in land-to-ocean MSE flux due to aerosol-induced surface turbulent flux changes are analogous to the seasonal transition triggered by shortwave radiation. During the seasonal transition from spring to summer when surface shortwave radiation increases over Eurasia and North America, surface turbulent flux increases, and also the MSE flux divergence due to stationary circulation increases (diamonds, Figs. 6a and b), exporting MSE from the land. Correspondingly, there is an increasing convergence of MSE flux due to stationary circulation in the ocean downstream (diamonds, Figs. 6d and e), indicating an increasing land-to-ocean MSE flux (Donohoe & Battisti, 2013). Note that also during the seasonal transition, the change of MSE flux divergence due to stationary circulation is greater over the Pacific sector (see also Fig. S5). Over the ocean sectors, the change in stationary circulations is compensated by transient eddies, espe-

cially over the Pacific (diamonds, Fig. 6d). The opposite is true for South and East Asia during the seasonal transition from fall to winter when surface shortwave radiation decreases (diamonds, Figs. 6c and f). There is a decrease of land-to-ocean MSE flux consistent with a decrease of surface turbulent flux over land upstream (see also Fig. S6), and compensation between stationary circulations and transient eddies over the ocean sector (diamonds, Fig. 6f). The compensation between stationary circulations and transient eddies during the NH seasonal cycle is consistent with previous work (Shaw et al., 2018; Barpanda & Shaw, 2020).

3.2.3 Aerosol-induced storm track trends

Next, we quantify how the trends in the atmospheric MSE budget affect the storm track weakening using Eq. (6). The storm track intensity, defined as $2\pi a \cos\phi F^{y,\star}_{TE}$, weakens significantly due to aerosol forcing (Fig. 7a). Similar to EKE and ECA trends (Fig. 2d and 3d), the weakening over the Pacific is greater than that in the Atlantic by 1.9 times (black, Fig. 7d). The spatial correlation between $2\pi a \cos\phi F^{y,\star}_{TE}$ trends and EKE and ECA trends due to aerosol forcing over 20–70°N are 0.67 and 0.65, respectively, supporting the use of regional MSE framework.

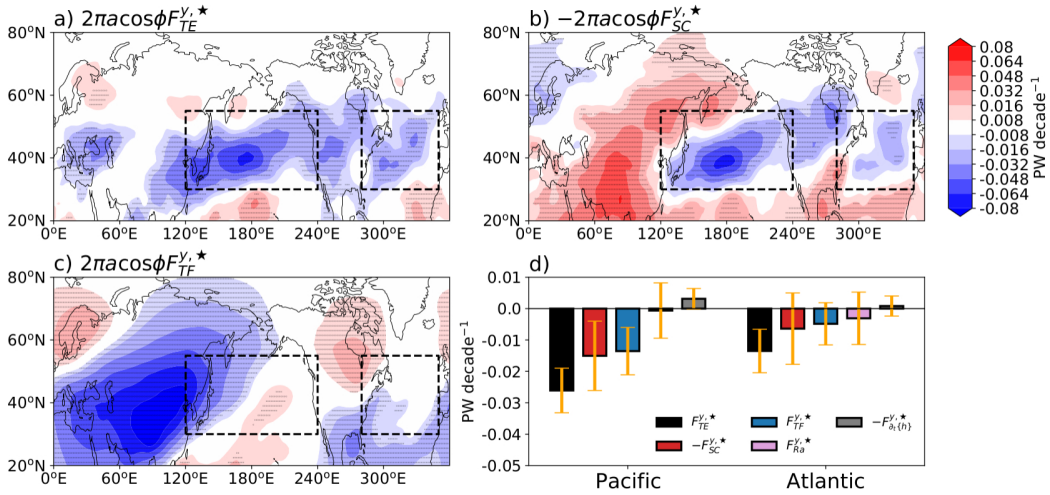

Figure 7. Spatial structure of JJA ensemble-mean trends from 1980 to 2020 of (a) storm track intensity ($2\pi a \cos\phi F^{y,\star}_{TE}$) and contributions from (b) stationary circulation ($-2\pi a \cos\phi F^{y,\star}_{SC}$) and (c) surface turbulent fluxes ($2\pi a \cos\phi F^{y,\star}_{TF}$) from the AER simulations. Statistically significant trends at the 95% confidence interval are stippled. The Pacific (30–55°N, 120–240°E) and Atlantic (30–55°N, 280–350°E) storm track domains are shown in black dashed box. (d) The ensemble-mean JJA storm track trends from 1980 to 2020 and their decomposition in the Pacific and Atlantic from the AER simulations. The 95% confidence intervals are shown with yellow errorbars. The $2\pi a \cos\phi$ factor is not labeled.

Since there is compensation between stationary circulations and transient eddies over the ocean (Fig. 5e and f), the stationary circulation is the dominant contributor to storm track weakening over the Pacific and Atlantic (Fig. 7b). Quantitatively, the stationary circulations contribute to 57.7% and 47.4% of the weakening over the Pacific and Atlantic, respectively (red, Fig. 7d). The surface turbulent flux also significantly contributes to the storm track weakening near the coastlines of upstream land (Fig. 7c). They contribute to 51.9% and 35.9% of the weakening over the Pacific and Atlantic, respectively (blue, Fig. 7d). Note also over southern and eastern Europe, the storm track weakening is dominated by surface turbulent flux contribution (Figs. 7a and c). While the contribution from the surface turbulent fluxes is maximized over land in East Asia (Fig. 7c), the storm track weakening there is not as strong since there is a strong cancellation from stationary circulation contribution (Fig. 7b). The contributions from radiative cooling and atmospheric storage are small for both storm tracks (pink and gray, Fig. 7d). The important contributions of stationary circulations and surface turbulent fluxes to storm track weakening are also found in reanalysis trends (Fig. S7).

The difference between the Pacific and Atlantic storm track trends is also contributed by both stationary circulations and surface turbulent fluxes. Two factors can be responsible for the difference. First is the difference in the positive surface shortwave radiation trends due to aerosol forcing over the land upstream, which are greater over Eurasian than North America. Second is the negative surface shortwave radiation trends due to aerosol forcing in the South and East Asia. To demonstrate the importance of the second factor, we investigate the trends during 41 years prior to the satellite era (1940–1980), when aerosol (shortwave-reflecting) emissions have been increasing in all NH land (Hoesly et al., 2018; Undorf et al., 2018). During this period when there is no surface shortwave trend dipole across Eurasia and South and East Asia, the storm track trends between the Pacific and Atlantic are comparable (Fig. S8).

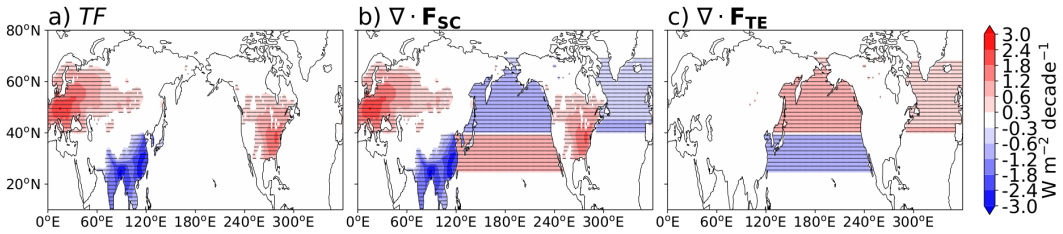

Figure 8. Spatial structure of JJA cosine-weighted trends from 1980 to 2020 in the theoretical model for (a) surface turbulent flux, (b) MSE flux divergence due to stationary circulations, and (c) MSE flux divergence due to transient eddies. The trends in (a) are taken from the AER simulations over Eurasia, North America, and South and East Asia. The slight difference between Fig. 5a and (a) is because the global-mean trend is removed in Fig. 5a. Statistically significant trends at the 95% confidence interval are stippled.

3.2.4 Prediction of aerosol-induced storm track trends

Building off of the dominant energetic balances seen in response to aerosol forcing, we build a theoretical model that uses the aerosol-induced surface turbulent flux trends to predict the storm track response. Recall the dominant atmospheric MSE budget trend balance over land (subscripted L) is between surface turbulent flux trends and MSE flux divergence trends due to stationary circulations (as shown in Figs. 6a–c), which is

$$\Delta TF_L = \Delta(\nabla \cdot \mathbf{F_{SC}})_L, \tag{7}$$

where Δ denotes the linear trend. In order to predict the downstream ocean (subscripted O) response we assume

$$\Delta(\nabla \cdot \mathbf{F_{SC}})_O = -\frac{A_L}{A_O}\Delta\langle\nabla \cdot \mathbf{F_{SC}}\rangle_L, \tag{8}$$

where $\langle\cdot\rangle$ represents an area average and A_L and A_O denote the area of upstream land and downstream ocean, respectively. Then, over the ocean, the dominant atmospheric MSE budget trend balance is between circulation components:

$$\Delta(\nabla \cdot \mathbf{F_{SC}})_O = -\Delta(\nabla \cdot \mathbf{F_{TE}})_O. \tag{9}$$

We consider three upstream land sectors (as in Figs. 6a–c), Eurasia (40–70°N), North America (30–60°N), and South and East Asia (10–40°N and 60–140°E) and three corresponding downstream ocean sectors (as in Figs. 6d–f), Pacific 40°–70°N, Atlantic 40°–70°N, and Pacific 25°–40°N. The selected upstream land and downstream ocean domains take into account the dominant pattern of land-to-ocean MSE flux trends due to aerosol forcing and their climatology (magenta and cyan lines in Figs. 5d and e). The predicted responses following Eqs. (7)–(9) show land-ocean energetic coupling (Fig. 8).

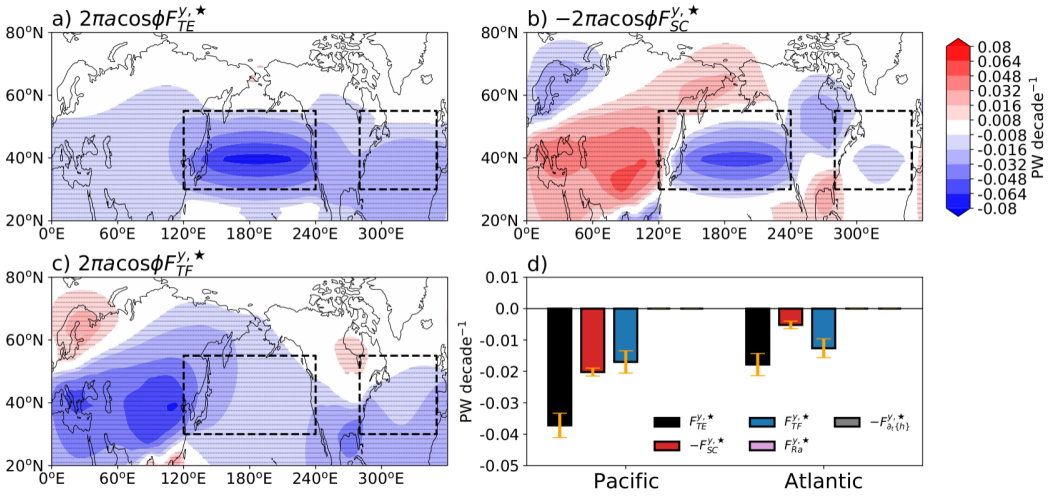

Figure 9. Similar results to Fig. 7, but for trends predicted from the theoretical model. In (d), the trends due to radiative cooling ($2\pi a\cos\phi F^{y,\star}_{Ra}$) and atmospheric heat storage ($-2\pi a\cos\phi F^{y,\star}_{\partial_t\{h\}}$) are zero.

The storm track trends predicted from the theoretical model exhibit weakening over the Pacific and Atlantic sectors (Fig. 9a) as in the AER simulations (Fig. 7a). Although slightly overestimated, the storm track trends from the theoretical model well resemble the spatial pattern of trends in the AER simulations with a spatial correlation coefficient of 0.60 over 20–70°N. The Pacific storm track weakens about 2.1 times more than the Atlantic storm track according to the prediction (compare black bars in Fig. 9d), consistent with the AER simulations (1.9 times, Figs. 7d). The slight overestimation can be related to applying Eq. (7) over South and East Asia where the radiative cooling trend is also important.

The relative contributions of stationary circulations (Fig. 9b) and surface turbulent fluxes (Fig. 9c) predicted by the theoretical model are consistent with AER simulations over the Pacific (Fig. 7d and Fig. 9d). In the Atlantic, the relative contributions are less consistent between theoretical models and AER simulations, but the trends in AER simulations are not statistically significant there (Fig. 7d and Fig. 9d). Overall, the similarities between the predicted trends and the actual AER simulation confirm that processes represented by Eqs. (7)–(9) accurately capture the storm track weakening from aerosol forcing.

Given the skill of the theoretical prediction, we can use it to understand what leads to greater storm track weakening in the Pacific than in the Atlantic in response to aerosol forcing. We first test the impact of aerosol forcing over South and East Asia by reducing the surface turbulent flux trends there by half. The resulting storm track trends still show greater weakening in the Pacific than in the Atlantic (Fig. 10a), but only by 1.6 times (as compared to 2.1 times in Fig. 9). We then test the impact of greater aerosol forcing over Eurasia than North America by additionally reducing the surface turbulent flux trends over Eurasia by half. When Eurasian aerosol forcing is halved, the storm track trends in the Pacific and Atlantic become more comparable (their ratio is 1.4, Fig. 10b). This indicates that larger aerosol-induced positive surface shortwave radiation trends over Eurasia than North America and negative surface shortwave radiation trends over South and East Asia both contribute to greater storm track weakening over the Pacific than the Atlantic.

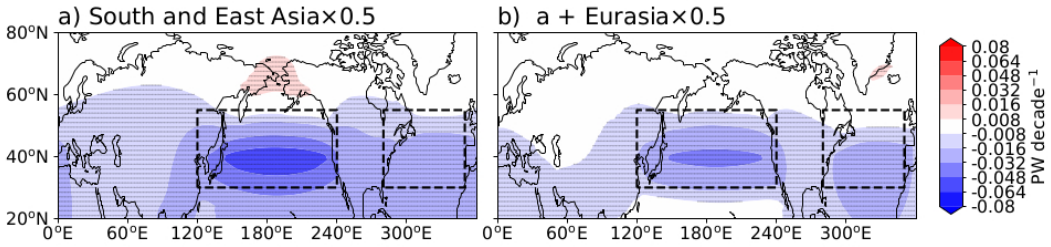

Figure 10. Similar results to Fig. 9a, but from theoretical model predictions (a) with aerosol forcing over South and East Asia reduced to half and (b) aerosol forcing over Eurasia also reduced to half. Statistically significant trends at the 95% confidence interval are stippled.

4 Summary and Discussions

The summertime regional circulation in the NH has significantly weakened during the satellite era with important implications for extreme weather. Here we quantify the drivers of the regional circulation weakening and employ an energetic framework to understand the underlying mechanisms. We focus on answering the questions raised in the introduction. The answer to the first series of questions is that anthropogenic aerosols

and greenhouse gas forcings contribute roughly equally to regional circulation weakening in the satellite era according to single-forcing DAMIP simulations. Moreover, the storm track weakening from anthropogenic aerosol forcing is about two times greater in the Pacific than in the Atlantic. This regional impact of aerosol forcing makes it the leading contributor to storm track weakening in the Pacific (about 54%), consistent with its impact on the upper-level Eurasian jet stream (Undorf et al., 2018; Dong et al., 2022).

The answer to the second series of questions is that aerosol-induced shortwave radiation trends over land weaken the storm tracks by driving changes in land-to-ocean energy transport. The increasing surface shortwave radiation trends (dominated by clear-sky radiation) due to decreasing aerosol emissions over Eurasia and North America are balanced by increasing surface turbulent flux trends into the atmosphere. The stationary circulations act to diverge energy from land downstream to the ocean. The result is energy convergence due to stationary circulations poleward of the storm tracks, which weaken the storm track over the ocean. This process is about twice as strong in the Eurasia-Pacific sector than in the North America-Atlantic sector because emission trends are larger over Eurasia. Additionally, increasing aerosol emissions over South and East Asia lead to the opposite behavior: decreasing surface shortwave radiation and turbulent flux trends lead to stationary circulation trends that diverge energy equatorward of the Pacific storm tracks to weaken it.

We use the underlying energetic balances to create a theoretical model that predicts the storm track weakening trend given the surface turbulent flux trends over land. With this theoretical model, we show that greater negative emission trends over Eurasian than North America and positive aerosol emission trends over South and East Asia lead to larger storm track weakening over the Pacific. The importance of positive aerosol emission trends over South and East Asia for different circulation responses between the Pacific and Atlantic is consistent with previous work for annual mean temperature (Diao et al., 2021; Kang et al., 2021). While previous work noted that aerosol-induced negative shortwave trends over East Asia are overestimated in the CMIP6 models (Wang et al., 2021), our theoretical modeling approach suggests that the actual response can be predicted by rescaling the overestimated forcing. Our results also suggest that aerosol-radiation interactions are important for summertime Pacific storm track trends, unlike the wintertime when aerosol-cloud interaction is also important (Zhang et al., 2007; Wang et al., 2014).

The significant impact of aerosols on the summertime regional circulation is in agreement with previous work showing radiative changes over land results in fast climate response (Dong et al., 2022). Previous work also showed Arctic sea ice loss could not explain the recent summertime circulation weakening in the NH (Kang et al., 2023). Consistently there is negligible Arctic sea ice loss in response to aerosol forcing (Fig. S9).

Our regional energetic analysis highlights the importance of stationary circulations in shaping the response of the storm tracks to external forcing in the NH (Kaspi & Schneider, 2013; Barpanda & Shaw, 2017; Shaw et al., 2018). We note that storm track weakening due to aerosol forcing is analogous to storm track weakening during the seasonal transition from spring to summer, especially over the Pacific (Fig. S5). Both processes involve surface shortwave radiation changes balanced by surface turbulent fluxes, which induce a stationary circulation to export energy downstream on the poleward side of the storm tracks. The similarity of the mechanisms operating seasonally and in response to aerosol forcing suggests the possibility of an emergent constraint, something that will be investigated in future work.

The significant role of anthropogenic aerosols in shaping summertime circulation trends in the satellite era suggests that future summertime circulation will also depend on future emissions of anthropogenic aerosols (Persad et al., 2022). Moreover, since the circulation response to aerosol forcing is primarily through changes in shortwave radi-

ation, the results here provide valuable insights into understanding circulation changes under solar geoengineering scenarios (Gertler et al., 2020) and volcanic eruptions (DallaSanta et al., 2019).

Open Research Section

The CFSR reanalysis data are available at `https://www.ncei.noaa.gov/data/climate-forecast-system/access/reanalysis/` and `https://www.ncei.noaa.gov/data/climate-forecast-system/access/operational-analysis/`. The ERA5 reanalysis data are available at `https://cds.climate.copernicus.eu/cdsapp#!/dataset/reanalysis-era5-pressure-levels?tab=form`. JRA-55 reanalysis data can be downloaded from `https://rda.ucar.edu/datasets/ds628.0/`. MERRA-2 reanalysis data can be downloaded from `https://disc.gsfc.nasa.gov/datasets?project=MERRA-2`. The CMIP6 DAMIP simulations are downloadable from the CMIP6 data search interface `https://esgf-node.llnl.gov/search/cmip6/`. The datasets supporting the conclusion of this work are available at `https://doi.org/10.5281/zenodo.11188121`.

Acknowledgments
JMK, TAS, and LS are supported by NSF-AGS2300037.

References

Allen, R. J., & Sherwood, S. C. (2011). The impact of natural versus anthropogenic aerosols on atmospheric circulation in the community atmosphere model. *Climate dynamics*, *36*, 1959–1978.

Barpanda, P., & Shaw, T. (2017). Using the moist static energy budget to understand storm-track shifts across a range of time scales. *Journal of the Atmospheric Sciences*, *74*(8), 2427–2446.

Barpanda, P., & Shaw, T. A. (2020). Surface fluxes modulate the seasonality of zonal-mean storm tracks. *Journal of the Atmospheric Sciences*, *77*(2), 753–779.

Boos, W. R., & Korty, R. L. (2016). Regional energy budget control of the intertropical convergence zone and application to mid-Holocene rainfall. *Nature Geoscience*, *9*(12), 892–897.

Chang, E. K., Ma, C.-G., Zheng, C., & Yau, A. M. (2016). Observed and projected decrease in Northern Hemisphere extratropical cyclone activity in summer and its impacts on maximum temperature. *Geophysical Research Letters*, *43*(5), 2200–2208.

Chemke, R., & Coumou, D. (2024). Human influence on the recent weakening of storm tracks in boreal summer. *npj Climate and Atmospheric Science*, *7*(1), 86.

Coumou, D., Di Capua, G., Vavrus, S., Wang, L., & Wang, S. (2018). The influence of Arctic amplification on mid-latitude summer circulation. *Nature Communications*, *9*(1), 1–12.

Coumou, D., Lehmann, J., & Beckmann, J. (2015). The weakening summer circulation in the Northern Hemisphere mid-latitudes. *Science*, *348*(6232), 324–327.

DallaSanta, K., Gerber, E. P., & Toohey, M. (2019). The circulation response to volcanic eruptions: The key roles of stratospheric warming and eddy interactions. *Journal of Climate*, *32*(4), 1101–1120.

Danabasoglu, G., Lamarque, J.-F., Bacmeister, J., Bailey, D., DuVivier, A., Edwards, J., ... others (2020). The community earth system model version 2 (CESM2). *Journal of Advances in Modeling Earth Systems*, *12*(2), e2019MS001916.

Deser, C., Lehner, F., Rodgers, K. B., Ault, T., Delworth, T. L., DiNezio, P. N.,

... others (2020). Insights from Earth system model initial-condition large ensembles and future prospects. *Nature Climate Change*, *10*(4), 277–286.

Diao, C., Xu, Y., & Xie, S.-P. (2021). Anthropogenic aerosol effects on tropospheric circulation and sea surface temperature (1980–2020): separating the role of zonally asymmetric forcings. *Atmospheric Chemistry and Physics*, *21*(24), 18499–18518.

Dong, B., & Sutton, R. T. (2021). Recent trends in summer atmospheric circulation in the North Atlantic/European region: is there a role for anthropogenic aerosols? *Journal of Climate*, *34*(16), 6777–6795.

Dong, B., Sutton, R. T., Shaffrey, L., & Harvey, B. (2022). Recent decadal weakening of the summer Eurasian westerly jet attributable to anthropogenic aerosol emissions. *Nature communications*, *13*(1), 1–10.

Donohoe, A., & Battisti, D. S. (2013). The seasonal cycle of atmospheric heating and temperature. *Journal of Climate*, *26*(14), 4962–4980.

Eyring, V., Bony, S., Meehl, G. A., Senior, C. A., Stevens, B., Stouffer, R. J., & Taylor, K. E. (2016). Overview of the Coupled Model Intercomparison Project Phase 6 (CMIP6) experimental design and organization. *Geoscientific Model Development*, *9*(5), 1937–1958.

Gelaro, R., McCarty, W., Suárez, M. J., Todling, R., Molod, A., Takacs, L., ... others (2017). The Modern-Era Retrospective Analysis for Research and Applications, version 2 (MERRA-2). *Journal of Climate*, *30*(14), 5419–5454.

Gertler, C. G., O'Gorman, P. A., Kravitz, B., Moore, J. C., Phipps, S. J., & Watanabe, S. (2020). Weakening of the extratropical storm tracks in solar geoengineering scenarios. *Geophysical Research Letters*, *47*(11), e2020GL087348.

Gertler, C. G., & O'Gorman, P. A. (2019). Changing available energy for extratropical cyclones and associated convection in Northern Hemisphere summer. *Proceedings of the National Academy of Sciences*, *116*(10), 4105–4110.

Gillett, N. P., Shiogama, H., Funke, B., Hegerl, G., Knutti, R., Matthes, K., ... Tebaldi, C. (2016). The detection and attribution model intercomparison project (DAMIP v1. 0) contribution to CMIP6. *Geoscientific Model Development*, *9*(10), 3685–3697.

Harvey, B., Cook, P., Shaffrey, L., & Schiemann, R. (2020). The response of the Northern Hemisphere storm tracks and jet streams to climate change in the CMIP3, CMIP5, and CMIP6 climate models. *Journal of Geophysical Research: Atmospheres*, *125*(23), e2020JD032701.

Hersbach, H., Bell, B., Berrisford, P., Hirahara, S., Horányi, A., Muñoz-Sabater, J., ... others (2020). The ERA5 global reanalysis. *Quarterly Journal of the Royal Meteorological Society*, *146*(730), 1999–2049.

Hoesly, R. M., Smith, S. J., Feng, L., Klimont, Z., Janssens-Maenhout, G., Pitkanen, T., ... others (2018). Historical (1750–2014) anthropogenic emissions of reactive gases and aerosols from the Community Emissions Data System (CEDS). *Geoscientific Model Development*, *11*(1), 369–408.

Hoskins, B., & Hodges, K. (2019). The annual cycle of northern hemisphere storm tracks. part i: Seasons. *Journal of Climate*, *32*(6), 1743–1760.

Kang, J. M., Shaw, T. A., Kang, S. M., Simpson, I. R., & Yu, Y. (2024). Revisiting the reanalysis-model discrepancy in southern hemisphere winter storm track trends. *ESS Open Archive*. doi: 10.22541/essoar.171224128.81410474/v1

Kang, J. M., Shaw, T. A., & Sun, L. (2023). Arctic sea ice loss weakens Northern Hemisphere summertime storminess but not until the late 21st century. *Geophysical Research Letters*, *50*(9), e2022GL102301.

Kang, S. M., Held, I. M., Frierson, D. M., & Zhao, M. (2008). The response of the ITCZ to extratropical thermal forcing: Idealized slab-ocean experiments with a GCM. *Journal of Climate*, *21*(14), 3521–3532.

Kang, S. M., Xie, S.-P., Deser, C., & Xiang, B. (2021). Zonal mean and shift modes of historical climate response to evolving aerosol distribution. *Science Bulletin*,

66(23), 2405–2411.

Kaspi, Y., & Schneider, T. (2013). The role of stationary eddies in shaping midlatitude storm tracks. *Journal of the atmospheric sciences*, *70*(8), 2596–2613.

Klimont, Z., Smith, S. J., & Cofala, J. (2013). The last decade of global anthropogenic sulfur dioxide: 2000–2011 emissions. *Environmental Research Letters*, *8*(1), 014003.

Kobayashi, S., Ota, Y., Harada, Y., Ebita, A., Moriya, M., Onoda, H., ... others (2015). The JRA-55 reanalysis: General specifications and basic characteristics. *Journal of the Meteorological Society of Japan. Ser. II*, *93*(1), 5–48.

Lehmann, J., & Coumou, D. (2015). The influence of mid-latitude storm tracks on hot, cold, dry and wet extremes. *Scientific Reports*, *5*(1), 1–9.

Leibensperger, E. M., Mickley, L. J., & Jacob, D. J. (2008). Sensitivity of US air quality to mid-latitude cyclone frequency and implications of 1980–2006 climate change. *Atmospheric Chemistry and Physics*, *8*(23), 7075–7086.

Ming, Y., & Ramaswamy, V. (2009). Nonlinear climate and hydrological responses to aerosol effects. *Journal of Climate*, *22*(6), 1329–1339.

Ming, Y., Ramaswamy, V., & Chen, G. (2011). A model investigation of aerosol-induced changes in boreal winter extratropical circulation. *Journal of climate*, *24*(23), 6077–6091.

Needham, M. R., & Randall, D. A. (2023). Anomalous northward energy transport due to anthropogenic aerosols during the twentieth century. *Journal of Climate*, *36*(19), 6713–6728.

Nicknish, P. A., Chiang, J. C., Hu, A., & Boos, W. R. (2023). Regional tropical rainfall shifts under global warming: an energetic perspective. *Environmental Research: Climate*, *2*(1), 015007.

O'Gorman, P. A. (2010). Understanding the varied response of the extratropical storm tracks to climate change. *Proceedings of the National Academy of Sciences*, *107*(45), 19176–19180.

Persad, G. G., Samset, B. H., & Wilcox, L. J. (2022). Aerosols must be included in climate risk assessments. *Nature*, *611*(7937), 662–664.

Pfleiderer, P., Schleussner, C.-F., Kornhuber, K., & Coumou, D. (2019). Summer weather becomes more persistent in a 2° C world. *Nature Climate Change*, *9*(9), 666–671.

Quaas, J., Jia, H., Smith, C., Albright, A. L., Aas, W., Bellouin, N., ... others (2022). Robust evidence for reversal of the trend in aerosol effective climate forcing. *Atmospheric Chemistry and Physics*, *22*(18), 12221–12239.

Saha, S., Moorthi, S., Pan, H.-L., Wu, X., Wang, J., Nadiga, S., ... others (2010). The NCEP climate forecast system reanalysis. *Bulletin of the American Meteorological Society*, *91*(8), 1015–1058.

Saha, S., Moorthi, S., Wu, X., Wang, J., Nadiga, S., Tripp, P., ... others (2014). The NCEP climate forecast system version 2. *Journal of climate*, *27*(6), 2185–2208.

Sardeshmukh, P. D., & Hoskins, B. I. (1984). Spatial smoothing on the sphere. *Monthly weather review*, *112*(12), 2524–2529.

Schmidt, G. (2013). *On mismatches between models and observations.* `https://www.realclimate.org/index.php/archives/2013/09/on-mismatches-between-models-and-observations/`. (Accessed: 04 September 2023)

Schumacher, D. L., Singh, J., Hauser, M., Fischer, E. M., Wild, M., & Seneviratne, S. I. (2024). Exacerbated summer European warming not captured by climate models neglecting long-term aerosol changes. *Communications Earth & Environment*, *5*(1), 182.

Shaw, T. A., Barpanda, P., & Donohoe, A. (2018). A moist static energy framework for zonal-mean storm-track intensity. *Journal of the Atmospheric Sciences*, *75*(6), 1979–1994.

Shaw, T. A., Miyawaki, O., & Donohoe, A. (2022). Stormier Southern Hemisphere

induced by topography and ocean circulation. *Proceedings of the National Academy of Sciences*, *119*(50), e2123512119.

Shaw, T. A., & Smith, Z. (2022). The Midlatitude Response to Polar Sea Ice Loss: Idealized Slab-Ocean Aquaplanet Experiments with Thermodynamic Sea Ice. *Journal of Climate*, *35*(8), 2633–2649.

Shaw, T. A., & Voigt, A. (2015). Tug of war on summertime circulation between radiative forcing and sea surface warming. *Nature Geoscience*, *8*(7), 560–566.

Shaw, T. A., & Voigt, A. (2016). Land dominates the regional response to CO_2 direct radiative forcing. *Geophysical Research Letters*, *43*(21), 11–383.

Shen, Z., & Ming, Y. (2018). The influence of aerosol absorption on the extratropical circulation. *Journal of Climate*, *31*(15), 5961–5975.

Undorf, S., Bollasina, M., & Hegerl, G. (2018). Impacts of the 1900–74 increase in anthropogenic aerosol emissions from North America and Europe on Eurasian summer climate. *Journal of Climate*, *31*(20), 8381–8399.

Wang, Y., Jiang, J. H., & Su, H. (2015). Atmospheric responses to the redistribution of anthropogenic aerosols. *Journal of Geophysical Research: Atmospheres*, *120*(18), 9625–9641.

Wang, Y., Wang, M., Zhang, R., Ghan, S. J., Lin, Y., Hu, J., ... Molina, M. J. (2014). Assessing the effects of anthropogenic aerosols on Pacific storm track using a multiscale global climate model. *Proceedings of the National Academy of Sciences*, *111*(19), 6894–6899.

Wang, Z., Lin, L., Xu, Y., Che, H., Zhang, X., Zhang, H., ... Xie, B. (2021). Incorrect Asian aerosols affecting the attribution and projection of regional climate change in CMIP6 models. *npj Climate and Atmospheric Science*, *4*(1), 2.

Xie, S.-P., Lu, B., & Xiang, B. (2013). Similar spatial patterns of climate responses to aerosol and greenhouse gas changes. *Nature Geoscience*, *6*(10), 828–832.

Zhang, R., Li, G., Fan, J., Wu, D. L., & Molina, M. J. (2007). Intensification of Pacific storm track linked to Asian pollution. *Proceedings of the National Academy of Sciences*, *104*(13), 5295–5299.